

ARTICLE

Received 22 Apr 2014 | Accepted 26 Aug 2014 | Published 3 Oct 2014

DOI: 10.1038/ncomms6088

Dry-air-stable lithium silicide–lithium oxide core-shell nanoparticles as high-capacity prelithiation reagents

Jie Zhao¹, Zhenda Lu¹, Nian Liu², Hyun-Wook Lee¹, Matthew T. McDowell¹ & Yi Cui^{1,3}

Rapid progress has been made in realizing battery electrode materials with high capacity and long-term cyclability in the past decade. However, low first-cycle Coulombic efficiency as a result of the formation of a solid electrolyte interphase and Li trapping at the anodes, remains unresolved. Here we report $\text{Li}_x\text{Si-Li}_2\text{O}$ core-shell nanoparticles as an excellent prelithiation reagent with high specific capacity to compensate the first-cycle capacity loss. These nanoparticles are produced via a one-step thermal alloying process. $\text{Li}_x\text{Si-Li}_2\text{O}$ core-shell nanoparticles are processible in a slurry and exhibit high capacity under dry-air conditions with the protection of a Li_2O passivation shell, indicating that these nanoparticles are potentially compatible with industrial battery fabrication processes. Both Si and graphite anodes are successfully prelithiated with these nanoparticles to achieve high first-cycle Coulombic efficiencies of 94% to >100%. The $\text{Li}_x\text{Si-Li}_2\text{O}$ core-shell nanoparticles enable the practical implementation of high-performance electrode materials in lithium-ion batteries.

¹Department of Materials Science and Engineering, Stanford University, Stanford, California 94305, USA. ²Department of Chemistry, Stanford University, Stanford, California 94305, USA. ³Stanford Institute for Materials and Energy Sciences, SLAC National Accelerator Laboratory, 2575 Sand Hill Road, Menlo Park, California 94025, USA. Correspondence and requests for materials should be addressed to Y.C. (email: yicui@stanford.edu).

Rechargeable lithium-ion batteries are widely used for consumer electronics and exhibit great potential for electrical vehicle and grid-scale energy storage^{1–4}. The first charging process, in which lithium ions and electrons move from cathode to anode, is critical for lithium-ion battery operation. When the potential of the anode is below ~ 1 V versus Li metal, the organic electrolyte is reduced on the anode surface to form a layer of solid electrolyte interphase (SEI) that consists of a complex composition of inorganic and organic lithium compounds^{5–8}. In addition, some lithium may be trapped in the electrode upon lithiation⁹. As a result, the first charging process irreversibly consumes a fraction of the lithium ions, giving rise to a net loss of storage capacity. Such first-cycle irreversible capacity loss is usually compensated by additional loading of cathode materials in current lithium-ion batteries. However, lithium metal-oxide cathodes have much lower specific capacity (mostly less than ~ 200 mAh g⁻¹) than anodes^{3,10}. Excessive loading of cathode material causes appreciable reduction of battery specific energy and energy density. It is therefore attractive to develop an alternative method that suppresses this loss and consequently increases the first-cycle Coulombic efficiency.

Addressing first-cycle capacity loss is an important step forward in the success of commercial graphite anodes. With graphite anodes, 5–20% of the lithium from the cathode is consumed to form the SEI, corresponding to an appreciable amount of inactivated cathode material. In the past two decades, the first-cycle Coulombic efficiency of graphite anodes has increased from $< 80\%$ to 90–95% through optimization of material quality, electrolyte and additives^{11–14}. Further improvement is likely to result from pre-compensation or prelithiation of the electrodes¹⁵.

Besides graphite anodes, prelithiation presents exciting opportunities for next-generation high-capacity anode materials such as Si, Ge and Sn, which have a large first-cycle capacity loss^{16,17}. For example, Si is a particularly attractive anode material, owing to its high specific capacity of $\sim 4,200$ mAh g⁻¹, excellent material abundance and well-developed industrial infrastructure for manufacturing^{16,18}. In the past several years, there has been exciting progress in addressing the issues associated with large volume change ($> 300\%$) during lithium insertion and extraction by designing nanostructured Si including nanowires and core-shell nanowires^{19–22}, hollow particles and tubes^{23–25}, porous materials^{26,27}, Si/C nanocomposites^{28–30} and by using novel binders^{31–34}. One of the remaining issues for Si anodes is the large capacity loss in the first cycle. The first-cycle Coulombic efficiency is typically very low, in the range of 50–80%^{31,35–37}, in spite of a few reports with higher values of $\sim 85\%$ ^{38,39}.

The first-cycle Coulombic efficiency can be improved by prelithiation. Anode prelithiation has been previously achieved by inducing electrical shorting between anode materials and lithium metal foil^{40,41}. It requires a temporary battery to be fabricated, a process that is difficult to scale up. In addition, prelithiation of a thick electrode with Li foil is time consuming, as it requires the diffusion of Li ions across the entire anode. Another approach is to use stabilized lithium metal powder (SLMP), which is effective to pre-compensate the first-cycle irreversible capacity loss of different anode materials, such as graphite and silicon-carbon nanotube (Si-CNT) composite^{15,42–44}. It is thus far the only prelithiation reagent in the powder form that can potentially be adopted during battery manufacturing, although practical challenges still exist to be addressed⁴⁵. It is therefore highly desirable to develop alternative microparticles or nanoparticles (NPs) for prelithiation.

Herein, we demonstrate that chemically synthesized core-shell NPs of Li_xSi–Li₂O (Fig. 1) as an excellent prelithiation reagent,

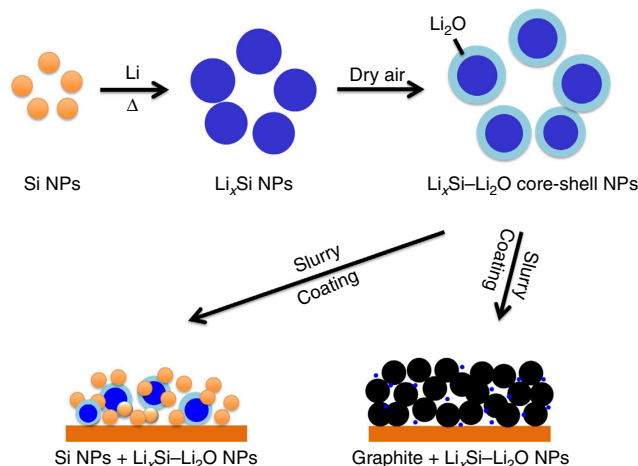


Figure 1 | Schematic diagrams showing Si NPs react with melted Li to form Li_xSi NPs. A dense passivation layer is formed on the Li_xSi NPs after exposure to trace amounts of oxygen, preventing the Li_xSi alloy from further oxidation in dry air. As-synthesized Li_xSi–Li₂O core-shell NPs, compatible with the existing battery-manufacturing environment, can be mixed with various anode materials during slurry processing and serve as an excellent prelithiation reagent.

which can be mixed with various anode materials during slurry processing. Li_xSi NPs exhibit multiple attractive properties for prelithiation: (1) fully lithiated Li_xSi alloy has a sufficiently low potential of around 10 mV versus Li/Li⁺ to prelithiate all types of anodes including graphite, Si, Ge and Sn^{16,18,46}; (2) Li_xSi has very high specific capacity (4,200 mAh g⁻¹ of Si, 2,000 mAh g⁻¹ of Li_{4.4}Si) for pre-storing lithium, so only a small percentage of material is needed for prelithiation; (3) nanoscale Li_xSi–Li₂O particles (100–200 nm) are helpful for distributing pre-stored Li uniformly across the anodes. Furthermore, using nanoscale Li_xSi–Li₂O particles as prelithiation reagent is less likely to disturb the whole structure of the electrode⁴⁷; (4) nanoscale Li_xSi particles provide a localized lithium source to realize fast prelithiation of anode materials, compared with the process of inducing electrical shorting between anode materials and lithium metal foil; (5) potentially, Li_xSi can benefit from the mature manufacturing infrastructure of the Si industry for scale-up and low-cost manufacturing.

Another challenge associated with anode prelithiation is the high chemical reactivity of prelithiation reagents, which make them difficult to survive multiple processing steps (exposure to air and solvents, slurry mixing, coating and baking) during battery electrode fabrication. A protective coating is therefore needed. However, this coating needs to be activated later to ensure quick lithium-ion diffusion for prelithiation. Li_xSi is a very reactive prelithiation reagent. In this paper, we also studied how to protect and de-protect it using a Li_xSi–Li₂O core-shell nanostructure. The following findings in this paper are important to enable successful prelithiation: (1) The core-shell NPs rapidly react with solvents containing active protons such as water and alcohol. The slow reaction with oxygen, however, allows the formation of a dense Li₂O shell that protects the Li_xSi core in dry-air environments over the long term. This is exciting since these NPs are compatible with the low-humidity environment of a dry room, commonly used in existing battery manufacturing; (2) for solvents without active protons, we found that Li_xSi can survive in low-polarity solvents such as ether and toluene during slurry processing. Highly polar solvents such as *N*-methyl-2-pyrrolidinone and organic carbonate can weaken the protection of the Li₂O shell and react with the Li_xSi core, making them poor candidates for solvents in slurry

processing. At the end of the battery assembly process, carbonate electrolyte is injected, directly resulting in the activation of the facile lithium diffusion into anode materials. To the best of our knowledge, this is the first report on prelithiation of anode materials with stabilized Li_xSi NPs.

Results

Synthesis and characterizations of $\text{Li}_x\text{Si-Li}_2\text{O}$ NPs. Li_xSi NPs were synthesized by mechanical stirring of a stoichiometric mixture (1:4.4) of Si NPs (~ 50 nm in diameter) and Li metal foil at 200°C for 6 h in a glove box (Ar-atmosphere, H_2O level < 0.1 p.p.m. and O_2 level < 3 p.p.m.). In the process, the colour of the powder changes from brown to black, indicating the formation of the Li_xSi alloy. Owing to trace oxygen in the glove box, a dense Li_2O passivation layer will form outside the Li_xSi NPs, resulting in the formation of $\text{Li}_x\text{Si-Li}_2\text{O}$ core-shell NPs and preventing Li_xSi from further oxidizing. The Li_2O passivation layer was evidenced by extensive characterization. Transmission electron microscopy (TEM) images were taken immediately after exposure of the samples to the electron beam to minimize the impact of the electron beam on the NPs. The TEM image (Fig. 2a) and scanning electron microscopy (SEM) image (Supplementary Fig. 1a) show that the size of the Li_xSi NPs range from 100 to 200 nm, which is larger than the Si NPs (50 nm) due to volume expansion and some aggregation of particles during the alloying process. The magnified TEM image (Fig. 2b) shows a thin passivation layer (~ 10 nm thick) on the surface of the Li_xSi NPs.

Compositional analysis of the Li_xSi NPs was acquired by electron energy loss spectroscopy (EELS) in the TEM. EELS is ideal for Li mapping, since the shallow Li K-edge has a high-ionization cross-section, which is about 10–100 times greater than that of other light elements such as oxygen⁴⁸. Oxygen mapping is therefore performed with longer exposure time per step. Compared with the scanning transmission electron microscopy (STEM) image in Fig. 2c, the corresponding EELS oxygen map (Fig. 2d) reveals that oxygen is concentrated in the passivation layer of the core-shell NPs. To avoid possible beam damage through consecutive scans, a different region is selected for Li and Si mapping. STEM image (Fig. 2e) and corresponding EELS elemental mapping reveal the spatial distribution of Li (Fig. 2f) and Si (Fig. 2g), respectively. The specific electron energy loss

spectra of Li, Si and O are shown in Supplementary Fig. 2. According to the elemental maps, Li is distributed throughout the entire nanoparticle, whereas Si is distributed in the internal part of the nanoparticle. Both images and elemental maps suggest that the NPs form a core-shell structure, consisting of a core of Li_xSi and a shell of Li_2O . Furthermore, X-ray diffraction (XRD) of the product (Fig. 2h) reveals the crystalline nature of the core-shell NPs formed by $\text{Li}_{21}\text{Si}_5$ (PDF# 00-018-747) and Li_2O (PDF# 04-001-8930). The broad background comes from the Kapton tape used to protect the samples from moisture in the air. $\text{Li}_{21}\text{Si}_5$, a variation of the $\text{Li}_{22}\text{Si}_5$ phase with ordered vacancies, is the most thermally stable phase among the crystalline lithium silicides^{46,49}.

Electrochemical performance. To study the electrochemical properties of the $\text{Li}_x\text{Si-Li}_2\text{O}$ NPs, half cells were fabricated with Li metal as a counter electrode. LiPF_6 (1.0 M) in a mixture of 1:1 w/w ethylene carbonate/diethyl carbonate, 10 vol% fluor-ethylene carbonate and 1 vol% vinylene carbonate was used as the electrolyte. To find a proper solvent for the slurry process, $\text{Li}_x\text{Si-Li}_2\text{O}$ NPs were mixed with carbon black (Super P) and polyvinylidene fluoride (PVDF) (65:20:15 by weight) in different solvents to form a slurry, which was then drop cast on copper foil and dried under vacuum. The entire battery electrode preparation process from the slurry formation to drop casting and drying were performed in a dry-air glove box (dew point = -50°C). The capacities of the resulting electrodes were studied by delithiating the samples to 1 V directly. Figure 3a shows that there is almost no Li capacity extracted from the $\text{Li}_x\text{Si-Li}_2\text{O}$ NPs processed with *N*-methyl-2-pyrrolidinone solvent. With diethyl carbonate solvent, the $\text{Li}_x\text{Si-Li}_2\text{O}$ NPs show a small Li extraction capacity of ~ 300 mAh g^{-1} , indicating that most of the stored Li is not active. Excitingly, $\text{Li}_x\text{Si-Li}_2\text{O}$ NPs are compatible with 1,3-dioxolane (DOL) and toluene (Fig. 3a), showing high extraction capacities of 1,200–1,400 mAh g^{-1} , which is sufficient to qualify it as a prelithiation reagent. It appears the highly polar functional groups can be attacked by free electrons in Li_xSi acting as a nucleophile. The detailed reaction mechanism is shown in Supplementary Fig. 3. Notice that PVDF binder does not dissolve in toluene to form a uniform slurry, so DOL is selected in the following experiments.

To evaluate the electrochemical behaviour of the $\text{Li}_x\text{Si-Li}_2\text{O}$ NPs, normal deep galvanostatic lithiation/delithiation was used.

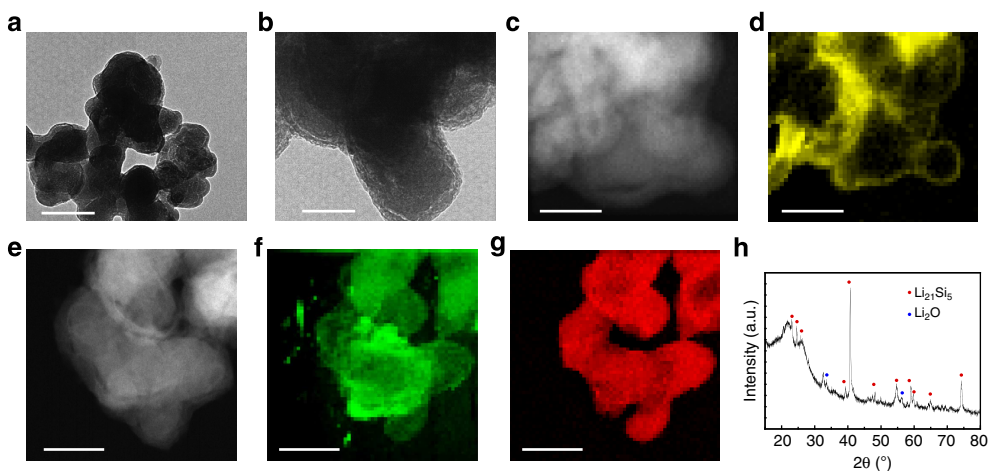


Figure 2 | Characterization of $\text{Li}_x\text{Si-Li}_2\text{O}$ core-shell NPs. (a) TEM image of $\text{Li}_x\text{Si-Li}_2\text{O}$ NPs. Scale bar, 200 nm. (b) Magnified TEM image reveals the core-shell nanostructure. (c) STEM image of $\text{Li}_x\text{Si-Li}_2\text{O}$ NPs, and (d) the corresponding EELS map of O distribution. Scale bar, 100 nm (b–d). (e) STEM image of $\text{Li}_x\text{Si-Li}_2\text{O}$ NPs. Corresponding EELS maps of (f) Li distribution and (g) Si distribution. Scale bar, 200 nm (e–g). (h) XRD pattern reveals the core-shell nanoparticles consisting of crystalline $\text{Li}_{21}\text{Si}_5$ and Li_2O .

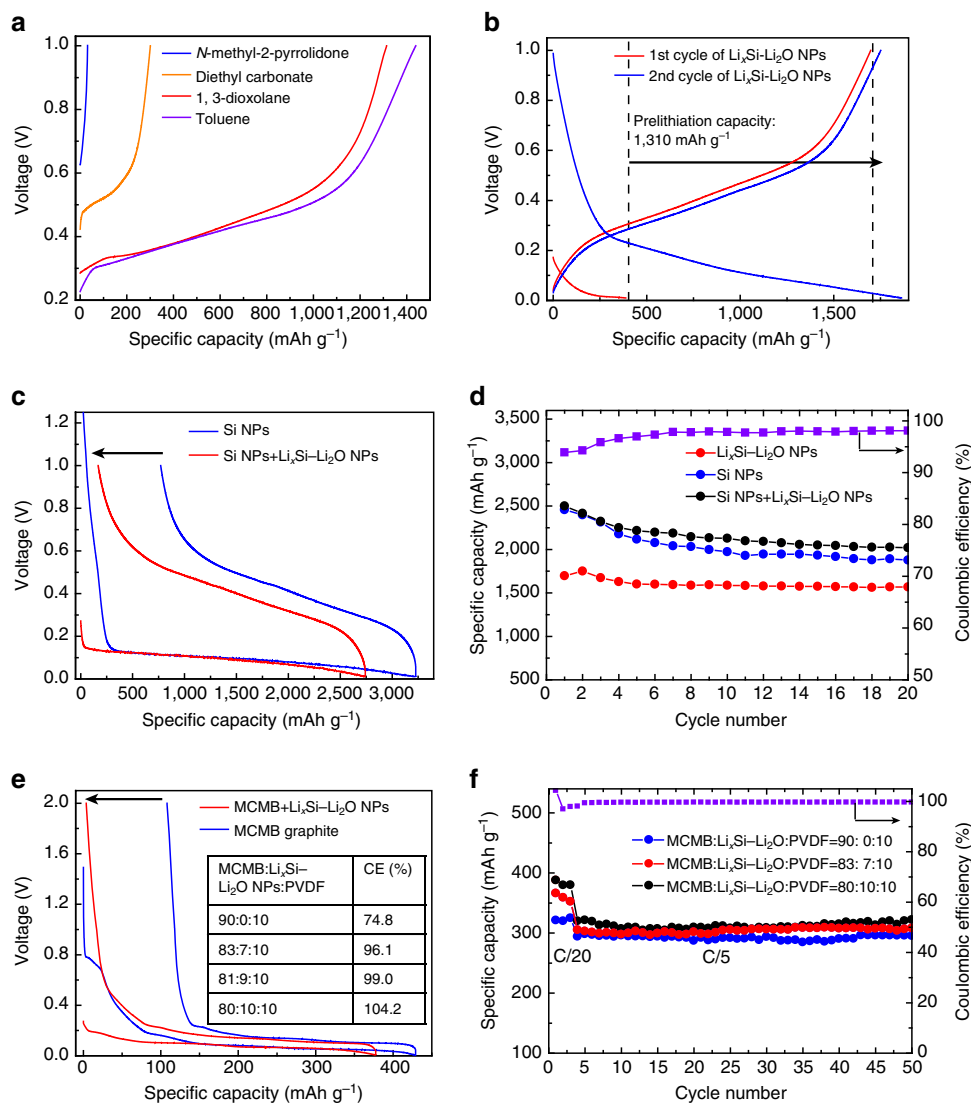


Figure 3 | Electrochemical characteristics. (a) First-cycle delithiation capacity of $\text{Li}_x\text{Si-Li}_2\text{O}$ NPs, using different solvents to form the slurry. (b) Galvanostatic discharge/charge profiles of $\text{Li}_x\text{Si-Li}_2\text{O}$ NPs in first and second cycles. (c) First-cycle voltage profiles of Si NPs/ $\text{Li}_x\text{Si-Li}_2\text{O}$ and Si NPs show that the incorporation of $\text{Li}_x\text{Si-Li}_2\text{O}$ additive compensates the first-cycle capacity loss of Si NPs. (d) Cycling performance of $\text{Li}_x\text{Si-Li}_2\text{O}$ NPs, Si NPs/ $\text{Li}_x\text{Si-Li}_2\text{O}$ and the control Si NPs at C/20 ($1\text{C} = 4.2 \text{ A g}^{-1} \text{ Si}$, the capacity is based on the total mass of Si in the electrodes). The purple line is the Coulombic efficiency of Si NPs/ $\text{Li}_x\text{Si-Li}_2\text{O}$ composite. (e) First-cycle voltage profiles of MCMB/ $\text{Li}_x\text{Si-Li}_2\text{O}$ (81:9 by weight) show $\text{Li}_x\text{Si-Li}_2\text{O}$ NPs improve the first-cycle Coulombic efficiency of MCMB. The table shows that the first-cycle Coulombic efficiency is tuned by the amount of $\text{Li}_x\text{Si-Li}_2\text{O}$ additives. (f) Cycling performance of MCMB/ $\text{Li}_x\text{Si-Li}_2\text{O}$ composites with different weight ratios at C/20 for first three cycles and C/5 for the following cycles ($1\text{C} = 0.372 \text{ A g}^{-1} \text{ C}$, the capacity is based on the mass of the total active materials, including MCMB and Si in $\text{Li}_x\text{Si-Li}_2\text{O}$ NPs). The purple line is the Coulombic efficiency of MCMB/ $\text{Li}_x\text{Si-Li}_2\text{O}$ composite (80:10 by weight).

Figure 3b shows the voltage profiles of the first and second cycles. $\text{Li}_x\text{Si-Li}_2\text{O}$ NPs were first lithiated to 0.01 V, and then delithiated to 1 V at a rate of C/20 (the specific capacity is calculated based on the mass of Si in the electrode. $1\text{C} = 4.2 \text{ A g}^{-1} \text{ Si}$). The open-circuit voltage (OCV) of $\text{Li}_x\text{Si-Li}_2\text{O}$ NPs was $<0.2 \text{ V}$, which is significantly lower than that of crystalline Si NPs. The capacity preloaded into Si NPs is $1,310 \text{ mAh g}^{-1}$, determined by subtracting the first lithiation capacity from the delithiation capacity. After the first cycle, the voltage profile is similar to normal Si anodes, but the second-cycle Coulombic efficiency of the $\text{Li}_x\text{Si-Li}_2\text{O}$ NPs is 96%, still higher than that of Si NPs (93%) (Supplementary Fig. 5a). During the slurry process, we believe that DOL will decompose on the surface of the $\text{Li}_x\text{Si-Li}_2\text{O}$ core-shell NPs to form a thin coating due to the strong reducing power of Li_xSi (Supplementary Fig. 1b). The reaction only consumes

part of the Li stored in the $\text{Li}_x\text{Si-Li}_2\text{O}$ NPs, and a significant amount of electrochemically active Li is left to be used as the pre-lithiation reagent.

Figure 3c demonstrates that $\text{Li}_x\text{Si-Li}_2\text{O}$ NPs can be used as a pre-lithiation reagent to improve the first-cycle Coulombic efficiency of normal Si NP anodes. The anodes were made by forming a slurry of Si NPs, $\text{Li}_x\text{Si-Li}_2\text{O}$ NPs, carbon black and PVDF binder with a mass ratio of 50:15:20:15. The dimensions of the $\text{Li}_x\text{Si-Li}_2\text{O}$ NPs are the same as that of Si NPs, so the $\text{Li}_x\text{Si-Li}_2\text{O}$ NPs were more uniformly distributed in the electrode compared with large-size pre-lithiation reagent. After a coin cell was fabricated, 6 h was needed for the anode to reach equilibrium. The first-cycle voltage profile reveals an OCV of 0.27 V, much lower than that of the control cell, which indicates partial pre-lithiation of the Si NPs. The capacity of the $\text{Li}_x\text{Si-Li}_2\text{O}$

NPs compensates the irreversible capacity loss of the Si NPs in the first cycle. Therefore, the first-cycle Coulombic efficiency increased from 76 to 94%. In addition, the lithiation capacity due to SEI formation decreases, due to the pre-formation of SEI during the prelithiation process. The electrochemical cycling performance was evaluated using deep lithiation/delithiation cycling from 1 to 0.01 V. The $\text{Li}_x\text{Si-Li}_2\text{O}$ NPs exhibited improved cycling performance over Si NPs at C/20 as displayed in Fig. 3d. Using $\text{Li}_x\text{Si-Li}_2\text{O}$ NPs as anode material, enough void space formed during the delithiation will be pre-built into the electrode structure to accommodate the volume expansion during the next lithiation process. Accordingly, the introduction of $\text{Li}_x\text{Si-Li}_2\text{O}$ NPs into Si NP anodes did not affect the cycling performance of Si NPs (the specific capacity was based on the total mass of Si in the electrode. $1\text{C} = 4.2\text{ A g}^{-1}\text{ Si}$). The cyclic voltammetry (CV) measurement of Si/ $\text{Li}_x\text{Si-Li}_2\text{O}$ NPs (Supplementary Fig. 4b) also demonstrates the performance of Si anode is negligibly affected by the addition of prelithiation reagents.

$\text{Li}_x\text{Si-Li}_2\text{O}$ NPs can also be used to compensate the irreversible capacity loss of existing graphite anodes as shown in the first-cycle voltage profiles (Fig. 3e). Graphite anodes consisting of mesocarbon microbeads (MCMB) graphite and a PVDF binder (90:10 by weight) were measured in a voltage window from 0.005 to 2 V as a control. In Fig. 3e, the blue voltage profile reveals a sloping region between 0.7 and 0.2 V, corresponding to SEI formation during first-cycle lithiation. As a result, the apparent first lithiation capacity of MCMB graphite is higher than the theoretical capacity of graphite (372 mAh g^{-1}), whereas the first-cycle Coulombic efficiency is just 75%. Prelithiation of the MCMB graphite by $\text{Li}_x\text{Si-Li}_2\text{O}$ NPs (mass ratio 81:9, red line) yields a first-cycle Coulombic efficiency of 99%. The electrochemical potential of the electrode is close to 0.3 V, indicating partial prelithiation of MCMB graphite. The incorporation of

$\text{Li}_x\text{Si-Li}_2\text{O}$ NPs decreases the typical lithiation capacity, due to the pre-formation of SEI during the prelithiation process. CV of MCMB/ $\text{Li}_x\text{Si-Li}_2\text{O}$ composites (blue) and MCMB graphite (red) shows consistent results (Supplementary Fig. 4c). As shown in the table in Fig. 3e, the first-cycle Coulombic efficiency of MCMB anodes can be adjusted by tuning the amount of $\text{Li}_x\text{Si-Li}_2\text{O}$ additive. The first-cycle Coulombic efficiency ranges from 96 to 104% by varying the mass ratio of MCMB to $\text{Li}_x\text{Si-Li}_2\text{O}$ NPs from 83:7 to 80:10. The MCMB/ $\text{Li}_x\text{Si-Li}_2\text{O}$ composites (mass ratio of 83:7 and 80:10) exhibited stable cycling performance at C/20 for the first three cycles and C/5 for the following cycles ($1\text{C} = 372\text{ mA g}^{-1}\text{ C}$) as displayed in Fig. 3f. The specific capacity was based on the mass of MCMB graphite and Si in the $\text{Li}_x\text{Si-Li}_2\text{O}$ additives. The capacities of MCMB/ $\text{Li}_x\text{Si-Li}_2\text{O}$ composites are slightly higher than that of the control graphite cell, contributed by the capacity stored in the $\text{Li}_x\text{Si-Li}_2\text{O}$ NPs. The incorporation of $\text{Li}_x\text{Si-Li}_2\text{O}$ NPs into the MCMB graphite electrode does not damage the structure of the electrode during cycling. As a result, the cycling performance of MCMB graphite is not affected. Furthermore, $\text{Li}_x\text{Si-Li}_2\text{O}$ additives also improve the second-cycle Coulombic efficiency of MCMB, and Coulombic efficiency of the subsequent cycles is comparable to cells without additives (Supplementary Fig. 5b). Prelithiation of graphite flakes by $\text{Li}_x\text{Si-Li}_2\text{O}$ NPs (mass ratio 83:7) shows consistent results, increased first-cycle coulombic efficiency from 87 to 99% (Supplementary Fig. 6a). Graphite/ LiFePO_4 full cells are used to investigate the effect of $\text{Li}_x\text{Si-Li}_2\text{O}$ particles on full cell performance. The SEM image and half-cell study of LiFePO_4 are shown in Supplementary Fig. 7. One full cell consists of graphite flake anode prelithiated with $\text{Li}_x\text{Si-Li}_2\text{O}$ particles (graphite flakes: $\text{Li}_x\text{Si-Li}_2\text{O}$:PVDF = 83:7:10), whereas another one consists of an anode with regular graphite flakes (graphite flakes: PVDF = 90:10). The cells are measured in the voltage

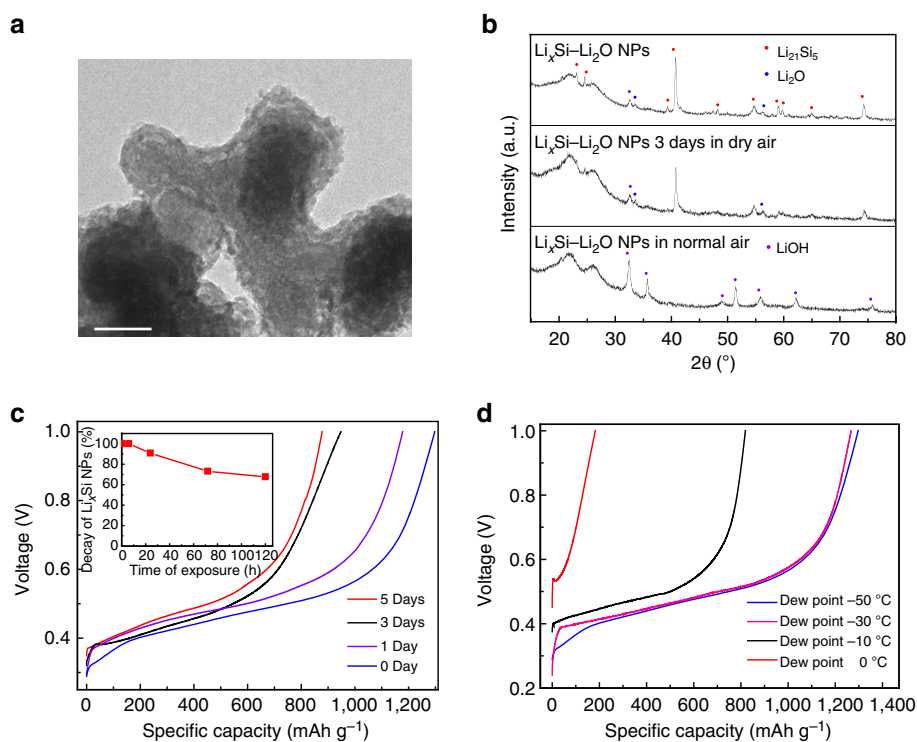


Figure 4 | Stability of $\text{Li}_x\text{Si-Li}_2\text{O}$ NPs. (a) TEM image of $\text{Li}_x\text{Si-Li}_2\text{O}$ NPs after 3 days of exposure to dry air. Scale bar, 100 nm. (b) XRD patterns of $\text{Li}_x\text{Si-Li}_2\text{O}$ NPs without exposure to dry air, exposed to dry air for 3 days and under ambient conditions. (c) The capacity retention of $\text{Li}_x\text{Si-Li}_2\text{O}$ NPs exposed to dry air with varying durations. The inset shows the trend of capacity decay. (d) The capacity retention of $\text{Li}_x\text{Si-Li}_2\text{O}$ NPs exposed to air at different humidity levels.

window from 2.5 to 3.8 V at C/10 (Supplementary Fig. 8a). The rate and cell capacity are both presented based on the mass of LiFePO₄ in the cathode. The blue voltage profile reveals a plateau between 2.6 and 3.2 V, corresponding to the SEI formation in the anode during charging. After incorporating Li_xSi–Li₂O particles into the anode, the OCV before cycling is about 2.3 V, significantly higher than 0.8 V for regular full cell. As shown by the red voltage profile, the incorporation of Li_xSi–Li₂O NPs compensates the irreversible Li consumption resulting from SEI formation. Accordingly, the first-cycle Coulombic efficiency increases from 77.6 to 90.8%. In the following cycles, the cell with Li_xSi–Li₂O NPs consistently shows a higher capacity than the regular cell (Supplementary Fig. 8b).

Stability of Li_xSi–Li₂O NPs. Figure 4a is a TEM image to show that the Li_xSi–Li₂O core-shell nanostructure remains after 3 days of exposure to dry air (dew point = –50 °C), although a thicker passivation layer of ~20 nm is observed, as compared with the original 10-nm-thick layer. XRD (Fig. 4b) analysis confirms that the sample exposed to dry air for 3 days is still composed of crystalline Li₂₁Si₅ and Li₂O. There is no obvious change in the XRD pattern as compared with the sample without exposure to dry air. The capacities of the Li_xSi–Li₂O NPs exposed to dry air for different numbers of days were studied by delithiating the Li_xSi–Li₂O NPs to 1 V directly (Fig. 4c). After exposure to dry air for 1 day, there is 1,175 mAh g^{–1} capacity, only a 9% decay from time zero. After 5 days of exposure, the Li_xSi–Li₂O NPs still exhibit a capacity of 880 mAh g^{–1} (red line in Fig. 4c), showing high capacity retention of 70%. The capacity of the Li_xSi–Li₂O NPs decays slowly with exposure time. The Li_xSi–Li₂O NPs stored in dry air for various durations were added into MCMB graphite to optimize the first-cycle Coulombic efficiency (MCMB:Li_xSi–Li₂O NPs = 8:1 by weight). The corresponding cells were tested in the voltage window of 0.005–2 V. The first-cycle voltage profiles of the MCMB/Li_xSi–Li₂O composites (Supplementary Fig. 9b) indicate that Li_xSi–Li₂O NPs stored in dry air for 5 days are still active enough to prelithiate MCMB graphite, yielding a 20% improvement in the first-cycle Coulombic efficiency. More attractively, Li_xSi–Li₂O NPs exhibit excellent dry-air stability even at elevated temperatures. MCMB/Li_xSi–Li₂O composites baked at 45 °C for 1 h in dry air exhibit a first-cycle Coulombic efficiency of 101.6%. Li_xSi–Li₂O NPs after baking at 65 °C can still effectively prelithiate MCMB graphite to counteract the first-cycle capacity loss as shown in Supplementary Fig. 10. To test humidity stability, the Li_xSi–Li₂O NPs were stored in an air box with different dew points for 6 h. The capacity of the samples in air with different humidities was studied by discharging the samples to 1 V directly (Fig. 4d). The electrochemical performance demonstrates that 6 h of exposure to air with dew point of –30 °C does not affect the capacity. Even in air with a dew point of –10 °C, the Li_xSi–Li₂O NPs still exhibit a capacity of 819 mAh g^{–1}. However, the Li_xSi–Li₂O NPs were completely converted to LiOH under high humidity, as confirmed by the XRD pattern in Fig. 4b.

Discussion

Electrochemical characterization (Fig. 3b) shows that the amount of Li preloaded into the Si NPs is 1,310 mAh g^{–1} for Si. Li is partially consumed to form a Li₂O passivation layer to protect Li_xSi from further oxidation. During the slurry process, DOL decomposes on the surface of the NPs to form a thin layer due to the strong reducing power of Li_xSi, further consuming a fraction of the Li. However, the remaining capacity of the Li_xSi–Li₂O NPs is still sufficient as a prelithiation reagent, higher than most Li-rich cathode materials. Compared with the conventional approach of extra loading of cathode materials, prelithiation

using Li_xSi–Li₂O NPs more effectively increases the specific energy and energy density of batteries. Li_xSi–Li₂O core-shell NPs can be mixed with various anode materials in the slurry process to achieve high first-cycle Coulombic efficiency. Nanoscale Li_xSi particles provide uniform and localized Li distribution to realize fast prelithiation of anode materials. Cycling performance of anode materials is negligibly affected by the addition of prelithiation reagents. The low material loading and particle dimensions are less likely to disturb the structure of the electrode. In addition, void spaces will be formed through delithiation of the Li_xSi additive, which accommodates the volume expansion during the next lithiation process.

As shown in Fig. 4c, the capacity retention is 91% after exposure to dry air for 1 day indicating that the Li_xSi–Li₂O NPs are sufficiently stable to go through the battery fabrication process in a dry room. Li_xSi–Li₂O NPs exposed to dry air for 5 days are still active enough to prelithiate MCMB graphite, which yields a 20% improvement in the first-cycle Coulombic efficiency (red curve in Supplementary Fig. 9b), indicating the potential for long-term storage. We attribute the dry-air stability to the unique core-shell nanostructure. The dense Li₂O passivation layer has a remarkable effect in preventing Li_xSi NPs from thermally oxidizing in dry air. The stabilized Li_xSi NPs are still sensitive to moisture. Increasing the stability of the Li_xSi alloy in moisture is an important field for future investigations.

In summary, we have demonstrated a one-step thermal alloying process to synthesize Li_xSi–Li₂O core-shell NPs without using specialized capital equipment. These NPs exhibit high capacity under dry-air conditions with the protection of the Li₂O passivation shell, indicating that Li_xSi–Li₂O NPs are potentially compatible with industrial battery fabrication processes in a dry room. Both commercial Si NPs and graphite are prelithiated with Li_xSi–Li₂O NPs, thereby remarkably increasing the first-cycle Coulombic efficiency. It suppresses the undesired consumption of Li from cathode materials during SEI formation. The approach is generally applicable to various anode materials involving complex nanostructures. In addition, the Li_xSi alloy also serves as a new anode material with the potential to pair with all high-capacity lithium-free cathodes for next-generation high-energy-density lithium-ion batteries.

Methods

Synthesis of Li_xSi–Li₂O NPs. Si NPs (~50 nm, MTI Inc.) were dried under vacuum for 24 h to remove trapped water. Si NPs (140 mg) were mixed with 154 mg of Li metal foil (99.9%, Alfa Aesar). The Li_xSi NPs were synthesized by mixing the Si NPs and lithium foil at 200 °C under mechanical stirring for 6 h in a glove box (Ar-atmosphere, H₂O level <0.1 p.p.m. and O₂ level <3 p.p.m.).

Characterization. SEM and TEM images were taken using a FEI XL30 Sirion SEM and a FEI Tecnai G2 F20 X-TWIN, respectively. A FEI Titan 80–300 environmental TEM was employed for EELS mapping collection at an acceleration voltage of 300 kV. The energy resolution of the EELS spectrometer is about 0.9 eV as measured by the full width at half-maximum of the zero-loss peak. EELS mapping data was acquired using a C2 aperture size of 50 nm and a camera length of 48 mm. To minimize sample drift during the STEM EELS mapping, the mapping drift was corrected every 30 pixels. The energy window of the EELS was 40–145 eV for Li (Li K-edge, 54.7 eV) and Si (Si L_{2,3} edge 99.2 eV) peaks and 510–615 eV for O (O K-edge, 532 eV) peak. XRD patterns were obtained on a PANalytical X'Pert, Ni-filtered Cu K α radiation. Li_xSi NPs are sensitive to ambient moisture so the samples were sealed with Kapton tape (DuPont) in the glove box before XRD characterization.

Electrochemical measurements. Si NPs (~50 nm, MTI Inc.), MCMB graphite (MTI Inc.), carbon black (Super P, TIMCAL, Switzerland) and PVDF binder (Kynar HSV 900) were dried under vacuum for 24 h to remove trapped water. To prepare the working electrodes, various materials were dispersed uniformly in DOL to form a slurry. (Anode materials and mass ratio are based on specific cells.) The slurry was then cast onto a thin copper foil and dried under vacuum. Coin-type cells (2,032) were assembled in an Ar-filled glove box using a Li metal foil as counter/reference electrode. The electrolyte is 1.0 M LiPF₆ in 1:1 w/w ethylene

carbonate/DEC (EMD Chemicals), 1 vol % vinylene carbonate and 10 vol% fluor-ethylene carbonate (Novolyte Technologies). CV measurements were carried out on a BioLogic VMP3 system. Galvanostatic cycling was carried out using an MTT 8 Channel battery tester. The total mass loading of the Si-based anode was 0.7–1.0 mg cm⁻² and a typical total mass loading of the graphite-based anode was 2.0–2.5 mg cm⁻².

References

- Bruce, P. G., Freunberger, S. A., Hardwick, L. J. & Tarascon, J. M. Li-O₂ and Li-S batteries with high energy storage. *Nat. Mater.* **11**, 19–29 (2012).
- Tarascon, J. M. & Armand, M. Issues and challenges facing rechargeable lithium batteries. *Nature* **414**, 359–367 (2001).
- Whittingham, M. S. Lithium batteries and cathode materials. *Chem. Rev.* **104**, 4271–4301 (2004).
- Choi, N. S. *et al.* Challenges facing lithium batteries and electrical double-layer capacitors. *Angew. Chem. Int. Ed.* **51**, 9994–10024 (2012).
- Aurbach, D. *et al.* The study of electrolyte-solutions based on ethylene and diethyl carbonates for rechargeable Li batteries. 2. Graphite-electrodes. *J. Electrochem. Soc.* **142**, 2882–2890 (1995).
- Verma, P., Maire, P. & Novak, P. A review of the features and analyses of the solid electrolyte interphase in Li-ion batteries. *Electrochim. Acta* **55**, 6332–6341 (2010).
- Zhang, X. R., Kostecki, R., Richardson, T. J., Pugh, J. K. & Ross, P. N. Electrochemical and infrared studies of the reduction of organic carbonates. *J. Electrochem. Soc.* **148**, 1341–1345 (2001).
- Downie, L. E., Nelson, K. J., Petibon, R., Chevrier, V. L. & Dahn, J. R. The impact of electrolyte additives determined using isothermal microcalorimetry. *ECS Electrochem. Lett.* **2**, 106–109 (2013).
- Liu, N. *et al.* A pomegranate-inspired nanoscale design for large-volume-change lithium battery anodes. *Nat. Nanotech.* **9**, 187–192 (2014).
- Armand, M. & Tarascon, J. M. Building better batteries. *Nature* **451**, 652–657 (2008).
- Arakawa, M. & Yamaki, J. I. The cathodic decomposition of propylene carbonate in lithium batteries. *J. Electroanal. Chem.* **219**, 273–280 (1987).
- Matsumura, Y., Wang, S. & Mondori, J. Mechanism leading to irreversible capacity loss in Li ion rechargeable batteries. *J. Electrochem. Soc.* **142**, 2914–2918 (1995).
- Xu, K. Nonaqueous liquid electrolytes for lithium-based rechargeable batteries. *Chem. Rev.* **104**, 4303–4417 (2004).
- Wang, D. Y., Sinha, N. N., Petibon, R., Burns, J. C. & Dahn, J. R. A systematic study of well-known electrolyte additives in LiCoO₂/graphite pouch cells. *J. Power Sources* **251**, 311–318 (2014).
- Jarvis, C. R., Lain, M. J., Yakovleva, M. V. & Gao, Y. A prelithiated carbon anode for lithium-ion battery applications. *J. Power Sources* **162**, 800–802 (2006).
- Wu, H. & Cui, Y. Designing nanostructured Si anodes for high energy lithium ion batteries. *Nano Today* **7**, 414–429 (2012).
- Zhang, W. J. Lithium insertion/extraction mechanism in alloy anodes for lithium-ion batteries. *J. Power Sources* **196**, 877–885 (2011).
- McDowell, M. T., Lee, S. W., Nix, W. D. & Cui, Y. 25th Anniversary article: understanding the lithiation of silicon and other alloying anodes for lithium-ion batteries. *Adv. Mater.* **25**, 4966–4984 (2013).
- Chan, C. K. *et al.* High-performance lithium battery anodes using silicon nanowires. *Nat. Nanotech.* **3**, 31–35 (2008).
- Xie, J., Yang, X. G., Zhou, S. & Wang, D. W. Comparing one- and two-dimensional heteronanostructures as silicon-based lithium ion battery anode materials. *ACS Nano* **5**, 9225–9231 (2011).
- Jeong, S. *et al.* Etched graphite with internally grown Si nanowires from pores as an anode for high density Li-ion batteries. *Nano Lett.* **13**, 3403–3407 (2013).
- Sim, S., Oh, P., Park, S. & Cho, J. Critical thickness of SiO₂ coating layer on core@shell bulk@nanowire Si anode materials for Li-ion batteries. *Adv. Mater.* **25**, 4498–4503 (2013).
- Wu, H. *et al.* Stable cycling of double-walled silicon nanotube battery anodes through solid-electrolyte interphase control. *Nat. Nanotech.* **7**, 309–314 (2012).
- Yao, Y. *et al.* Interconnected silicon hollow nanospheres for lithium-ion battery anodes with long cycle life. *Nano Lett.* **11**, 2949–2954 (2011).
- Liu, N. *et al.* A yolk-shell design for stabilized and scalable Li-ion battery alloy anodes. *Nano Lett.* **12**, 3315–3321 (2012).
- Liu, N. A., Huo, K. F., McDowell, M. T., Zhao, J. & Cui, Y. Rice husks as a sustainable source of nanostructured silicon for high performance Li-ion battery anodes. *Sci. Rep.* **3**, 1919–1925 (2013).
- Ge, M. Y. *et al.* Large-scale fabrication, 3D tomography, and lithium-ion battery application of porous silicon. *Nano Lett.* **14**, 261–268 (2014).
- Jung, D. S., Hwang, T. H., Park, S. B. & Choi, J. W. Spray drying method for large-scale and high-performance silicon negative electrodes in Li-ion batteries. *Nano Lett.* **13**, 2092–2097 (2013).
- Hwang, T. H., Lee, Y. M., Kong, B. S., Seo, J. S. & Choi, J. W. Electrospun core-shell fibers for robust silicon nanoparticle-based lithium ion battery anodes. *Nano Lett.* **12**, 802–807 (2012).
- Magasinski, A. *et al.* High-performance lithium-ion anodes using a hierarchical bottom-up approach. *Nat. Mater.* **9**, 353–358 (2010).
- Wu, H. *et al.* Stable Li-ion battery anodes by in-situ polymerization of conducting hydrogel to conformally coat silicon nanoparticles. *Nat. Commun.* **4**, 1943–1948 (2013).
- Koo, B. *et al.* A highly cross-linked polymeric binder for high-performance silicon negative electrodes in lithium ion batteries. *Angew. Chem. Int. Ed.* **51**, 8762–8767 (2012).
- Wu, M. Y. *et al.* Toward an ideal polymer binder design for high-capacity battery anodes. *J. Am. Chem. Soc.* **135**, 12048–12056 (2013).
- Liu, G. *et al.* Polymers with tailored electronic structure for high capacity lithium battery electrodes. *Adv. Mater.* **23**, 4679–4683 (2011).
- Wu, H. *et al.* Engineering empty space between Si nanoparticles for lithium-ion battery anodes. *Nano Lett.* **12**, 904–909 (2012).
- Hu, L. B. *et al.* Silicon-conductive nanopaper for Li-ion batteries. *Nano Energy* **2**, 138–145 (2013).
- Yi, R., Dai, F., Gordin, M. L., Chen, S. R. & Wang, D. H. Micro-sized Si-C composite with interconnected nanoscale building blocks as high-performance anodes for practical application in lithium-ion batteries. *Adv. Energy Mater.* **3**, 295–300 (2013).
- Cui, L. F., Ruffo, R., Chan, C. K., Peng, H. L. & Cui, Y. Crystalline-amorphous core-shell silicon nanowires for high capacity and high current battery electrodes. *Nano Lett.* **9**, 491–495 (2009).
- Yao, Y., Liu, N., McDowell, M. T., Pasta, M. & Cui, Y. Improving the cycling stability of silicon nanowire anodes with conducting polymer coatings. *Energy Environ. Sci.* **5**, 7927–7930 (2012).
- Liu, N. A., Hu, L. B., McDowell, M. T., Jackson, A. & Cui, Y. Prelithiated silicon nanowires as an anode for lithium ion batteries. *ACS Nano* **5**, 6487–6493 (2011).
- Hassoun, J. *et al.* A contribution to the progress of high energy batteries: a metal-free, lithium-ion, silicon-sulfur battery. *J. Power Sources* **202**, 308–313 (2012).
- Forney, M. W. *et al.* Pre-lithiation of silicon-carbon nanotube anodes using stabilized lithium metal powder. *Nano Lett.* **13**, 4158–4163 (2013).
- Wang, Z. H. *et al.* Application of stabilized lithium metal powder (SLMP (R)) in graphite anode—a high efficient prelithiation method for lithium-ion batteries. *J. Power Sources* **260**, 57–61 (2014).
- Xiang, B., Wang, L., Liu, G. & Minor, A. M. Electromechanical probing of Li/Li₂CO₃ core/shell particles in a TEM. *J. Electrochem. Soc.* **160**, 415–419 (2013).
- Wang, L., Fu, Y. B., Battaglia, V. S. & Liu, G. SBR-PVDF based binder for the application of SLMP in graphite anodes. *RSC Adv.* **3**, 15022–15027 (2013).
- Wang, C. M. *et al.* In situ TEM Investigation of congruent phase transition and structural evolution of nanostructured silicon/carbon anode for lithium ion batteries. *Nano Lett.* **12**, 1624–1632 (2012).
- Harris, S. J. & Lu, P. Effects of inhomogeneities-nanoscale to mesoscale-on the durability of Li-ion batteries. *J. Phys. Chem. C* **117**, 6481–6492 (2013).
- Wang, F. *et al.* Chemical distribution and bonding of lithium in intercalated graphite: identification with optimized electron energy loss spectroscopy. *ACS Nano* **5**, 1190–1197 (2011).
- Nesper, R. & Vonscherner, H. G. Li₂Si₅, a zintl phase as well as a humerothery phase. *J. Solid State Chem.* **70**, 48–57 (1987).

Acknowledgements

Y.C. acknowledges the support from the Assistant Secretary for Energy Efficiency and Renewable Energy, Office of Vehicle Technologies of the US Department of Energy. H.-W.L. acknowledges support from the Basic Science Research Program through the National Research Foundation of Korea (NRF) funded by the Ministry of Education, Science and Technology under NRF-2012R1A6A3A03038593. M.T.M. acknowledges the National Science Foundation Graduate Fellowship Program and the Stanford Graduate Fellowship Program. We thank Dr Zheng Chen, Dr Zhidan Zeng, Dr Hongwei Zhou, Dr Kai Yan, Jian He, Dr Desheng Kong and Denys Zhuo for helpful discussion.

Author contributions

J.Z. and Y.C. conceived the concept. J.Z. carried out the synthesis and performed materials characterizations and electrochemical measurements. N.L., Z.L. and H.-W.L. conducted XRD, TEM and EELS mapping, respectively. M.T.M. inspired the synthesis method. J.Z., Z.L. and Y.C. co-wrote the paper. All authors discussed the results and commented on the manuscript.

Additional information

Supplementary Information accompanies this paper at <http://www.nature.com/naturecommunications>

Competing financial interests: The authors declare no competing financial interests.

Reprints and permission information is available online at <http://npg.nature.com/reprintsandpermissions/>

How to cite this article: Zhao, J. *et al.* Dry-air-stable lithium silicide–lithium oxide core–shell nanoparticles as high-capacity prelithiation reagents. *Nat. Commun.* 5:5088 doi: 10.1038/ncomms6088 (2014).